Multi-Receiver Random Access With Joint Position–Orientation–FOV Optimization for Uplink OWC Networks

Dengke Wang, *Member, IEEE*, Zhihong Zeng, *Member, IEEE*, Fengli Yang, *Member, IEEE*, Chen Chen, *Senior Member, IEEE*, Jia Ye, *Member, IEEE*, Xiping Wu, *Senior Member, IEEE*, and Harald Haas, *Fellow, IEEE*

***Abstract*—In this letter, we investigate uplink optical wireless random access in a symmetric four-photodiode (PD) receiver cell, where each PD is allowed to move along the ceiling diagonals and is jointly optimized in terms of its position, orientation, and field of view (FOV). To guarantee full observability of the coverage area, we first derive an analytical bound that characterizes the relationship among PD displacement, pointing direction, and the minimum FOV required for complete coverage. Leveraging this result, we propose a coverage-critical boundary optimization strategy that substantially reduces the search space for identifying the optimum. Based on a Lambertian channel model and an signal-to-interference plus noise ratio (SINR)-driven successive interference cancellation (SIC) decoding rule, simulation results confirm the existence of an optimal position–orientation–FOV triplet. In unobstructed environments, the optimal geometry places the PDs near the cell corners, and enabling orientation control—rather than adjusting the FOV alone with fixed PD positions—achieves up to a 37.5% throughput improvement over conventional designs.**

***Index Terms*—Uplink OWC, random access, multi-PD, optimization.**

I. Introduction

SHORT-RANGE optical wireless communication (OWC), including its high-capacity Light Fidelity (LiFi) variant, has emerged as a strong candidate to complement radio-frequency (RF) technologies in next-generation Internet-of-Things (IoT) networks [1], [2]. By operating in the unlicensed optical spectrum and exploiting the inherent directivity of optical propagation, OWC/LiFi systems offer high security, immunity to RF interference, and natural support for ultra-dense spatial reuse [3]. As IoT devices continue to proliferate in indoor environments, ranging from smart offices and warehouses to industrial automation and environmental monitoring, there is a growing demand for uplink mechanisms that provide reliable, low-latency, and interference-resilient connections [4].

Modern LiFi networks support bidirectional optical communication, with downlink transmission embedded into LED-based illumination and uplink realized via infrared (IR) emitters [5]. The downlink has advanced significantly through space-division multiple access (SDMA) techniques, which exploit angular diversity and attocell architectures to spatially separate users and improve multiplexing performance [6], [7]. Recent works further integrate Non-Orthogonal Multiple Access (NOMA) to enhance multiuser efficiency [8]. In contrast, the uplink benefits from centralized processing enabled by wired interconnections among PD receivers. This facilitates multi-receiver SIC, where spatially redundant observations across PDs improve collision resolution and throughput in random-access scenarios [9], [10], [11].

Recent advances have explored dynamic adaptation of receiver or antenna configurations to enhance spatial-domain performance [12], [13]. For instance, prior work has proposed dynamically adjusting each PD's FOV to regulate the connectivity of the RA graph and optimize throughput based on the instantaneous device activation probability [7], [10]. While such adaptive FOV shrinking can significantly improve the decodability of uplink packets under moderate loads, aggressive FOV reduction inevitably creates severe coverage holes. On the other hands, at high activation probabilities, the throughput-optimal configuration collapses each AP's coverage to only its nearest users while leaving the remaining area completely uncovered. However, practical OWC/LiFi deployments—whether for communication, illumination, or sensing—require uninterrupted service coverage across the entire target region. Therefore, strategies that maximize throughput by sacrificing spatial coverage are fundamentally incompatible with operational requirements in real deployments. Second, existing uplink RA models lack geometric realism. Prior studies typically assume idealized vertically oriented PDs with fixed FOVs and positions, neglecting the constraints introduced by real optical hardware, including allowable orientation angles, finite aperture size, and physical mounting restrictions. Downlink studies such as [6] clearly demonstrate that angular selectivity, beam orientation, and geometric layout critically shape interference patterns and spatial multiplexing options. Yet, to the best of our knowledge, no

Received 8 April 2026; revised 17 June 2026; accepted 28 August 2026. Date of publication 3 September 2026; date of current version 11 September 2026. This work was supported in part by the National Natural Science Foundation of China under Grant 62271091 and Grant 62501088; and in part by the Open Research Fund of National Mobile Communications Research Laboratory, Southeast University, under Grant 2026D08. The associate editor coordinating the review of this article and approving it for publication was Y. Xiao. *(Corresponding author: Zhihong Zeng.)*

Dengke Wang, Fengli Yang, and Chen Chen are with the School of Microelectronics and Communication Engineering, Chongqing University, Chongqing 400044, China (e-mail: dengke.wang@cqu.edu.cn; cqu_yfl@cqu.edu.cn; c.chen@cqu.edu.cn).

Zhihong Zeng is with the School of Microelectronics and Communication Engineering, Chongqing University, Chongqing 400044, China, and also with the National Mobile Communications Research Laboratory, Southeast University, Nanjing 210096, China (e-mail: zhihong.zeng@cqu.edu.cn).

Jia Ye is with the State Key Laboratory of Power Transmission Equipment Technology, School of Electrical Engineering, Chongqing University, Chongqing 400044, China (e-mail: j.ye@cqu.edu.cn).

Xiping Wu is with the National Mobile Communications Research Laboratory, School of Information Science and Engineering, Southeast University, Nanjing 211189, China, and also with Purple Mountain Laboratories, Nanjing 211111, China (e-mail: xiping.wu@seu.edu.cn).

Harald Haas is with the Department of Engineering, University of Cambridge, CB3 0FA Cambridge, U.K. (e-mail: huh21@cam.ac.uk).

Digital Object Identifier 10.1109/LWC.2026.3730508

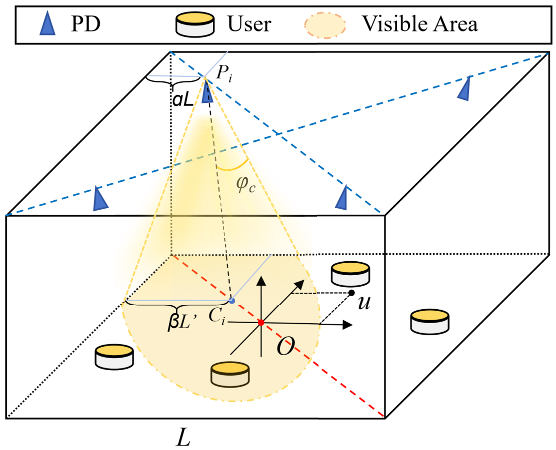

Fig. 1. Illustration of the system model, where the blue, black, and red dots denote the optical footprint center, the user location, and the coordinate origin, respectively.

existing uplink RA framework jointly considers PD position, orientation, FOV, indoor geometry, link-level optical channel characteristics, and SINR-driven multi-receiver SIC under a strict full-coverage requirement.

Motivated by these limitations, this work introduces a new uplink OWC framework that enforces strict full-area coverage while leveraging the benefits of spatial redundancy for SIC. Unlike prior adaptive-FOV approaches, our design guarantees that the entire region remains covered at all times. The resulting spatial structure—defined jointly by orientation, FOV, and geometry—creates controlled overlaps among the PDs' optical footprints. Specifically, the position of each PD is adjusted along a predefined spatial trajectory, while its orientation is controlled by a single-axis rotation mechanism to steer its receiving direction [13]. The FOV is determined by an adjustable optical hood [10]. Within this architecture, we derive the expression of the critical FOV with a given PD position and orientation for full-coverage, and propose a coverage-critical boundary optimization strategy, which greatly reduces the searching range of the joint position-orientation–FOV optimization under coverage constraints. Our results provide new insights into the geometry–interference–decodability tradeoff governing uplink OWC random access and reveal globally optimal configurations.

II. System Geometry and Channel Model

In this work, we consider an uplink OWC system in which four ceiling-mounted photodiodes (PDs) form a symmetric square enclosure around a target indoor region, which is a square coverage region of side length L, as illustrated in Fig. 1. Each PD is equipped with adjustable position, orientation, and FOV, enabling controlled spatial overlap among their optical footprints while maintaining full-area coverage and maximum network performance. To impose geometric symmetry, the system is modeled in a Cartesian coordinate frame where the center of the square region is located at the origin $(0,0,0)$, the x- and y-axes span the horizontal plane, and the z-axis points upward. The room is modeled as $\mathcal{S} = \left[-L/2, L/2\right] \times \left[-L/2, L/2\right]$, and the ceiling lies at height $z = h$. The four PDs are positioned diagonally with respect to the center.[1] To express this compactly, we define the index set

$$\mathcal{I} = \{(s,t) \mid s \in \{-1,+1\},\ t \in \{-1,+1\}\}, \tag{1}$$

representing the four combinations of diagonal directions in the xy-plane. Each PD is associated with one pair $(s_i, t_i) \in \mathcal{I}$. Using a normalized placement factor $\alpha \in [0, 1/2]$, the PD coordinates are written as

$$P_i = \left(s_i \left(\frac{1}{2} - \alpha\right) L,\ t_i \left(\frac{1}{2} - \alpha\right) L,\ h \right). \tag{2}$$

Analogously, the optical boresight of PD i is directed toward a designated footprint-center point, which we similarly constrain to lie along the diagonals. Let $\beta \in [0, 1]$ denote a normalized footprint-center factor. Then the footprint center for PD i is given by

$$C_i = (s_i\,(1-\beta)L,\ t_i\,(1-\beta)L,\ 0). \tag{3}$$

This definition yields a unique boresight vector determined by $\boldsymbol{b}_i = C_i - P_i$. The footprint size is controlled by the FOV half-angle ψ_{c}, which allows the designer to regulate coverage extent and the degree of spatial overlap among PDs for multi-receiver interference cancellation.

Users are assumed to be uniformly distributed on the horizontal plane $z = 0$ and access the network following a slotted ALOHA (SA) protocol, with an average λ of users per slot. A user indexed by j is located at $\boldsymbol{u}_j = (x, y, 0)$ and transmits upward with fixed power P_t, with its emission direction aligned with the positive z-axis.[2]

The j-th user is covered by PD i if the incidence angle satisfies $\psi_{i,j} \le \psi_{\mathrm{c}}$. Under the line of sight (LoS) Lambertian model in [14], the optical channel gain from user j to PD i is

$$h_{i,j} = \frac{A_c\,\rho_c\,\rho_t\,(m+1)}{2\pi \|\boldsymbol{v}_{i,j}\|^2}\,\cos^m(\phi_{i,j})\,\kappa(\psi_{i,j})\,\cos(\psi_{i,j}), \tag{4}$$

where ρ_c is the responsivity of PD, representing the current per unit of incident optical power (A/W), ρ_t is the electro-optic conversion factor of the transmitter (W/A), set to unity in our setting, A_c is the detection area, $\|\boldsymbol{v}_{i,j}\| = \|P_i - \boldsymbol{u}_j\|$ is the link distance, $\phi_{i,j}$ is the radiation angle, and $\kappa(\psi_{i,j}) = T_s(\psi_{i,j})\,g(\psi_{i,j})$, where $T_s(\psi_{i,j})$ is the optical filter gain and $g(\psi_{i,j}) = \nu^2/\sin^2(\psi_{\mathrm{c}})$ is the optical concentrator gain for $0 \le \psi_{i,j} \le \psi_{\mathrm{c}}$, with ν denoting the refractive index of the optical concentrator and ψ_{c} denoting half-angle FOV of the PD. The Lambertian order is $m = -\ln 2/\ln(\cos \Phi_{1/2})$, with $\Phi_{1/2}$ denoting the LED half-power semi-angle. $\psi_{i,j}$ denotes the incidence angle at the i-th PD.

A packet transmitted by user j is decodable at PD i if its instantaneous SINR exceeds a threshold γ_{th}, namely

$$\gamma_{ij} = \frac{P_t\,h_{ij}^2}{\sum\limits_{k \ne i} P_t\,h_{kj}^2 + N_0 B}, \tag{5}$$

[1] Diagonal symmetry is adopted to ensure balanced quadrant-wise coverage under random user distribution and to reduce optimization dimensionality.

[2] We adopt an averaged orientation for analytical tractability. More general models accounting for random device orientations can be found in [3].

where N_0 is the noise power spectral density and B is the system bandwidth. Due to the partially overlapping optical footprints across the PDs, each user packet may be received with different SINR levels at different PDs. This spatial diversity enables multi-receiver SIC in a manner analogous to the use of temporal diversity in coded random access schemes [15], while providing additional interference cancellation gains through geometry-induced power imbalance. Once a packet is decoded at any PD, it is removed from all interference sets and SINRs are re-evaluated across the PDs. The SIC process continues until either all packets are decoded or no packet exceeds the decoding threshold.

III. Full-Coverage Geometric Constraint of FOV and Coverage-Critical Boundary Optimization

In this section, we first derive the full-coverage FOV constraint, which characterizes the relationship among PD position, orientation, and the minimum FOV required for complete coverage. Based on this, we formulate a unified optimization problem to maximize the system throughput under geometric constraints, and then develop a corresponding optimization strategy.

A. Full-Coverage Geometric Constraint of FOV

We first exploit symmetry to reduce the coverage analysis to a single PD and two representative subsquares. Because the four PDs are placed and oriented in a diagonally symmetric fashion, the square region $\mathcal{S}$ can be partitioned into four congruent subsquares that are mapped to each other by 90° rotations and reflections. Therefore, it suffices to characterize the worst-case incidence angles within the near and diagonal subsquares of this representative PD; the other three PDs follow by symmetry.

Without loss of generality, we focus on the reference PD with sign pair $(s,t) = (-1,-1)$; the other PDs follow by symmetry. In the (x,y)-plane, we define $\mathcal{S}_{\mathrm{N}}$ and $\mathcal{S}_{\mathrm{D}}$ as the near cell and the diagonal cell of a given PD, respectively. These regions are specified as follows

$$\mathcal{S}_{\mathrm{N}} = \left[-\tfrac{L}{2}, 0\right] \times \left[-\tfrac{L}{2}, 0\right], \qquad \mathcal{S}_{\mathrm{D}} = \left[0, \tfrac{L}{2}\right] \times \left[0, \tfrac{L}{2}\right]. \quad (6)$$

Let $\psi_{i,j} = \psi(\boldsymbol{u};\alpha,\beta)$ denote the incidence angle at the i-th PD. By the cosine formula for the angle, we obtain

$$\cos\big(\psi_{i,j}\big) = \frac{\boldsymbol{b}_i^{\top}\boldsymbol{v}_{i,j}}{\|\boldsymbol{b}_i\|\,\|\boldsymbol{v}_{i,j}\|}, \quad (7)$$

where $\boldsymbol{b}_i$ is the boresight direction of PD i and $\boldsymbol{v}_{i,j}$ is the line-of-sight vector from PD i to user j. Substituting (2) and (3) into the cosine formula yields, using $s_i^2 = t_i^2 = 1$,

$$\cos\psi_{i,j} = \frac{(\beta'-\alpha')L\,(s_i x + t_i y - 2\alpha' L) + h^2}{\|\boldsymbol{b}_i\|\,\|\boldsymbol{v}_{i,j}\|}, \quad (8)$$

with $\|\boldsymbol{b}_i\| = \sqrt{2(\beta'-\alpha')^2L^2+h^2}$ and $\|\boldsymbol{v}_{i,j}\| = \sqrt{(x-s_i\alpha' L)^2 + (y-t_i\alpha' L)^2 + h^2}$. Here the auxiliary variables $\alpha' \triangleq \frac{1}{2} - \alpha \in [0,1/2]$ and $\beta' \triangleq 1-\beta \in [0,1]$ are introduced for notational brevity.

The FOV half-angle must be no smaller than the maximum incidence angle over that region, i.e.,

$$\psi_{\mathrm{c}} \geq \min_{r\in\{\mathrm{N},\mathrm{D}\}} \max_{\boldsymbol{u}_j\in\mathcal{S}_r} \psi_{i,j}. \quad (9)$$

The minimization over $r \in \{\mathrm{N},\mathrm{D}\}$ arises from the diagonal symmetry of the four-PD architecture. However, evaluating (9) directly entails a continuous maximization over a two-dimensional region, which is computationally inefficient. In the following, we establish a key lemma showing that the maximum incidence angle over $\mathcal{S}_r$ is attained at a finite set of representative boundary points, thereby enabling a closed-form and low-complexity characterization of the critical FOV.

Lemma 1: [Critical FOV for a diagonally symmetric PD with joint position–orientation design] In the four-PD diagonally symmetric receiver architecture, the entire square region $\mathcal{S}$ is fully covered if the common FOV half-angle satisfies $\psi_{\mathrm{c}} \geq \psi_{\mathrm{crit}}(\alpha,\beta)$, where the critical FOV is compactly defined as

$$\psi_{\mathrm{crit}}(\alpha,\beta) = \min_{r\in\{\mathrm{N},\mathrm{D}\}} \max_{\boldsymbol{u}\in\mathcal{U}_r} \psi(\boldsymbol{u};\alpha,\beta). \quad (10)$$

Here, $\mathcal{U}_{\mathrm{N}} = \{(0,0,0),\ (-L/2,0,0),\ (-L/2,-L/2,0)\}$, and $\mathcal{U}_{\mathrm{D}} = \{(L/2,L/2,0),\ (L/2,0,0),\ (0,0,0)\}$ denote the three representative vertices of the near and diagonal cells.

Proof: We first establish the convexity of the optical footprint. Since $\cos(\cdot)$ is strictly decreasing on $[0,\pi]$, the footprint can be equivalently written as the superlevel set $\mathcal{F}(\alpha,\beta,\psi_c) = \{(x,y) : \cos\psi(x,y;\alpha,\beta) \geq \cos\psi_c\}$. From (8), the cosine of the incidence angle has the form $\cos\psi = f(x,y)/g(x,y)$, where the numerator is an affine function in (x,y) and the denominator is a positive convex function, with

$$g(x,y) \geq h\sqrt{2(\beta'-\alpha')^2L^2+h^2} > 0$$

guaranteed by $h>0$. For any $\mathbf{u}_1,\mathbf{u}_2 \in \mathcal{F}$ and $\lambda\in[0,1]$, let $\mathbf{u}_\lambda = \lambda\mathbf{u}_1 + (1-\lambda)\mathbf{u}_2$. By the affinity of f and the superlevel set condition, we have $f(\mathbf{u}_\lambda) = \lambda f(\mathbf{u}_1) + (1-\lambda) f(\mathbf{u}_2)$, and

$$f(\mathbf{u}_\lambda) \geq c[\lambda g(\mathbf{u}_1) + (1)-\lambda) g(\mathbf{u}_2)] \geq c\, g(\mathbf{u}_\lambda),$$

where $c = \cos\psi_c$ and the last inequality follows from the convexity of g. Hence $\mathbf{u}_\lambda \in \mathcal{F}$, and the footprint is convex.

Since both S_N and S_D are squares, hence convex polygons, and the footprint $\mathcal{F}$ is convex, the sub-cell S_r is fully covered, i.e., $S_r \subseteq \mathcal{F}$, if and only if all vertices of S_r lie in $\mathcal{F}$. Specifically, the vertex sets of S_N and S_D are

$$V_N = \left\{(0,0),\ \left(-\tfrac{L}{2},0\right),\ \left(0,-\tfrac{L}{2}\right),\ \left(-\tfrac{L}{2},-\tfrac{L}{2}\right)\right\}, \quad (11)$$
$$V_D = \left\{(0,0),\ \left(\tfrac{L}{2},0\right),\ \left(0,\tfrac{L}{2}\right),\ \left(\tfrac{L}{2},\tfrac{L}{2}\right)\right\}. \quad (12)$$

From (8), i.e., for the PD with $s_i = t_i = -1$, the expression of the incidence-angle is symmetric under the interchange $x \leftrightarrow y$, i.e., $\psi(x,y;\alpha,\beta) = \psi(y,x;\alpha,\beta)$. so that $\psi(x,y;\alpha,\beta) = \psi(y,x;\alpha,\beta)$. Consequently, the vertex pairs $(-L/2,\ 0)$, $(0,\ -L/2)$ in S_N and $(L/2,\ 0)$, $(0,\ L/2)$ in S_D yield identical incidence angles. Removing one redundant vertex from each pair gives the representative sets U_N and U_D. The critical FOV half-angle is therefore $\psi_{\mathrm{crit}}(\alpha,\beta) = \min\{\max_{\mathbf{u}\in U_N}\psi(\mathbf{u};\alpha,\beta),\ \ \max_{\mathbf{u}\in U_D}\psi(\mathbf{u};\alpha,\beta)\}$, and the entire region $\mathcal{S}$ is fully covered if and only if $\psi_c \geq \psi_{\mathrm{crit}}$ (α,β). ■

TABLE I
SIMULATION PARAMETERS

Parameter	Value
Transmit power, P_t	50 mW
Detection area of PD, A_c	1 cm^2
Optical filter gain, T_s	0.92
Responsivity of PD, ρ_c	0.4 $\mathrm{A{\cdot}W^{-1}}$
Electro-optic conversion factor, ρ_t	1 $\mathrm{W{\cdot}A^{-1}}$
Refractive index of optical concentrator, ν	1.51
Noise power, N_0B	-115 dBm
Decoding threshold, γ_{th}	6 dB

B. Coverage-Critical Boundary Optimization

In this letter, we aim to maximize the throughput (R) over the full region by jointly optimizing the PD positions, orientations, and FOV parameter. The corresponding optimization problem is formulated as

$$\max_{\alpha,\beta,\psi_{\text{c}}} \quad R = \lambda\, P(\alpha,\beta,\psi_{\text{c}}|\lambda)$$
$$\text{s.t.} \quad \alpha \in \left[0, \tfrac{1}{2}\right],\ \beta \in [0,1],\ \psi_{\text{c}} \geq \psi_{\text{crit}}(\alpha,\beta). \qquad (13)$$

where $P(\alpha,\beta,\psi_{\text{c}}|\lambda)$ is the successful probability given average number of users. Although the optimal $(\alpha,\beta,\psi_{\text{c}})$ can be obtained by exhaustive search, its complexity is prohibitive; therefore, we develop a boundary-based optimization with reduced complexity. Through numerical investigation, we observe that the throughput-optimal FOV consistently lies near the coverage-critical boundary. This is consistent with the underlying interference–coverage tradeoff: reducing ψ_c below ψ_{crit} violates the full-coverage constraint, while increasing ψ_c far beyond ψ_{crit} admits excessive interference that degrades SIC performance. Motivated by this observation, we propose a boundary-based heuristic that restricts the search to the vicinity of the critical FOV boundary. Specifically, for each candidate pair (α,β) on a two-dimensional grid, the critical FOV ψ_{crit} is first computed using the vertex-based formula in Lemma 1; the throughput is then evaluated at $\psi_c = \psi_{\text{crit}}(\alpha,\beta)$ to identify the best pair $(\alpha^\star,\beta^\star)$; finally, starting from $\psi_c = \psi_{\text{crit}}(\alpha^\star,\beta^\star)$, a one-dimensional search over $\psi_c \geq \psi_{\text{crit}}(\alpha^\star,\beta^\star)$ refines the optimal FOV. This approach reduces the computational complexity from $\mathcal{O}(N_\alpha N_\beta N_\psi)$ to $\mathcal{O}(N_\alpha N_\beta + N_\psi)$, effectively eliminating one dimension from the exhaustive search, while achieving performance nearly identical to that of the brute-force global optimum, as validated in Fig. 5.

IV. SIMULATION RESULTS

The simulations are conducted over a square network area with side length $L = 5$ m, where the vertical distance between the transmitter plane and the receiver plane is $h = 3$ m. Users are uniformly distributed within the room, and the total number of active users in each slot follows a Poisson process with mean activity rate λ. Unless otherwise specified, the default simulation parameters are summarized in Table I. As the performance metric, we adopt the average number of successfully decoded users per slot, referred to as the normalized throughput.

We first evaluate the critical FOV required to guarantee full coverage under different PD positions and orientations. As illustrated in Fig. 2, when the optical footprint center is located at the corner ($\beta = 0$), a relatively large FOV (e.g., $\psi_c \geq 50°$) is required. As β increases and the footprint center moves toward the center of the square, the critical FOV decreases because the boresight becomes better aligned with the center of the near cell, reducing the maximum incidence angle. When β exceeds approximately 0.5, the critical FOV increases again, as the coverage requirement transitions from the near cell to the diagonal cell, which introduces a larger angular deviation. For sufficiently large β, however, the critical FOV decreases once more, since the PD is primarily responsible for covering the diagonal cell, whose geometry imposes a less stringent angular constraint. On the other hand, different PD projection positions lead to distinct trends in the critical FOV.

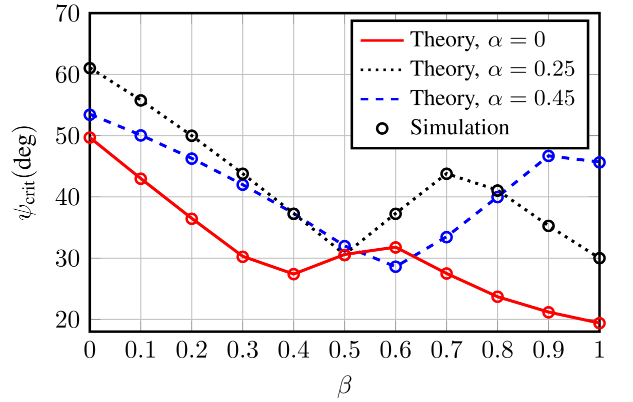

Fig. 2. Critical FOV vs. geometric parameters (α,β).

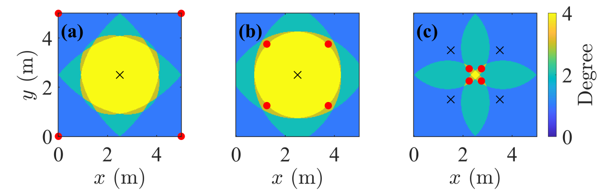

Fig. 3. Optical coverage degree map.

To better illustrate the underlying geometric mechanisms, we present Fig. 3, where the color scale indicates the number of PDs simultaneously covering each location. (a) $\alpha = 0$, $\beta = 1$, $\psi_{\text{c}} = 19.4°$; (b) $\alpha = 0.25$, $\beta = 1$, $\psi_{\text{c}} = 30°$; (c) $\alpha = 0.45$, $\beta = 0.6$, $\psi_{\text{c}} = 28.7°$; the red and black markers indicate the PD ground projections and optical footprint centers, respectively. This visualizes the optical geometry under different parameter settings. When the PD is located at the corner of the region ($\alpha = 0$), the dominant constraint is imposed by the diagonal cell. In this case, steering the PD boresight toward the center, i.e., adopting a larger inclination angle, such as $\beta = 1$, results in a wider optical footprint and consequently reduces the critical FOV. A similar behavior is observed for the intermediate placement $\alpha = 0.25$. In contrast, when the PD is positioned closer to the center of the room ($\alpha \to 0.5$), the critical FOV is instead determined by the near cell, as illustrated in Fig. 3(c).

Fig. 4 illustrates the maximum throughput as a function of the PD projection factor α, under different average numbers of active users λ. In this figure, red circle markers indicates the optimal operating point $\alpha^\star$. The orientation $\beta^\star$ and FOV

TABLE II
OPTIMAL OPERATING POINTS AND CORRESPONDING THROUGHPUT UNDER DIFFERENT SYSTEM CONFIGURATIONS

$\Phi_{1/2}$	λ	$\alpha^\star$	$\beta^\star$	$\psi_c^\star$ (deg)	Throughput
30°	3	0	0.2	33	2.450
30°	6	0	0.2	40	3.216
60°	3	0.05	0	57	2.007
60°	6	0	0	50	1.925

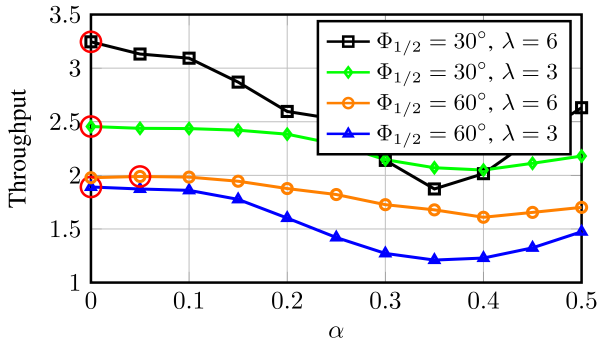

Fig. 4. The maximized throughput vs. PD position α.

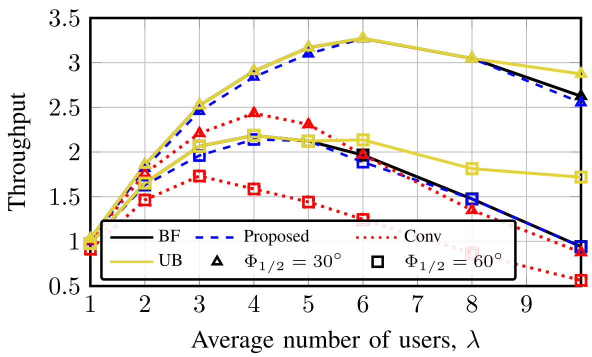

Fig. 5. Maximized throughput vs. average number of users λ.

$\psi_c^\star$ are jointly optimized for each α and listed in Table II. It is observed that the optimal PD projection consistently concentrates near $\alpha \approx 0$, indicating that placing the four PDs as far apart as possible is beneficial. Such a configuration enlarges the received power disparity across different PDs, thereby enhancing SIC effectiveness and improving the throughput.

Fig. 5 compares the throughput under different strategies, including the full-coverage constrained global search by brute-force (BF), the unconstrained (coverage-free) throughput-optimal upper bound (UB) by brute-force, the proposed optimization based on the boundary, and the adaptive FOV scheme in [10], where all PDs are placed at the centers of their respective sub-cells and oriented vertically downward, with only the FOV dynamically adjusted to optimize the throughput. It can be observed that the proposed method consistently achieves throughput values close to those of the constrained BF across the entire load range, with a gap of about 5% at $\lambda = 3$ for $\Phi_{1/2} = 60°$ and less than 3% for $\Phi_{1/2} = 30°$. The UB coincides with the proposed full-coverage design across the light and moderate load range, and exceeds it only under heavy load, where large coverage holes are tolerated to reduce interference, while significantly outperforming the conventional fixed configuration. Specifically, when $\Phi_{1/2} = 30°$, the proposed scheme attains a peak throughput of approximately 3.3, corresponding to a performance improvement of approximately 37.5% over the conventional scheme. When $\Phi_{1/2} = 60°$, an improvement of about 29.4% is obtained. These results demonstrate that the proposed boundary optimization provides near-optimal performance with substantially reduced computational complexity.

V. CONCLUSION

We introduced an angle-constrained, fully covered, multi-PD cooperative uplink OWC design that jointly optimizes PD position, orientation, and FOV, integrating Lambertian geometry, a derived critical-FOV bound for full coverage, a low-complexity boundary optimization strategy, and SINR-driven SIC. Simulation results verify the existence of optimal geometric–optical parameters, outperforming existing schemes that do not enforce geometric coverage constraints, while guaranteeing full coverage at only a marginal throughput cost relative to an unconstrained upper bound. This work opens opportunities for spatial design in future OWC IoT systems.

REFERENCES

[1] M. Liu, H. Kazemi, M. Safari, I. Tavakkolnia, and H. Haas, "A comprehensive comparison between terahertz and optical wireless communications," *Npj Wireless Technol.*, vol. 1, no. 1, p. 3, Nov. 2025.

[2] D. Wang, T. Chu, Z. Zeng, C. Chen, M. Liu, and H. Haas, "Joint trajectory-energy design for integrated satellite-terrestrial networks with hybrid light/RF energy harvesting," *IEEE J. Sel. Areas Commun.*, vol. 44, pp. 4833–847, 2026.

[3] A. Memedi and F. Dressler, "Vehicular visible light communications: A survey," *IEEE Commun. Surveys Tuts.*, vol. 23, no. 1, pp. 161–181, 1st Quart., 2021.

[4] S. Bastiaens, M. Alijani, W. Joseph, and D. Plets, "Visible light positioning as a next-generation indoor positioning technology: A tutorial," *IEEE Commun. Surveys Tuts.*, vol. 26, no. 4, pp. 2867–2913, 2024.

[5] Z. Zeng et al., "Interference mitigation using optimized angle diversity receiver in LiFi cellular network," *Opt. Commun.*, vol. 574, p. 131125, Apr. 2025.

[6] Z. Chen, D. A. Basnayaka, and H. Haas, "Space division multiple access for optical attocell network using angle diversity transmitters," *J. Lightw. Technol.*, vol. 35, no. 11, pp. 2118–2131, Jun. 1, 2017.

[7] M. D. Soltani, I. Tavakkolnia, and H. Haas, "Interference reduction in LiFi using an optical receiver with dynamic FoV," in *Proc. IEEE 101st Veh. Technol. Conf. (VTC-Spring)*, Jun. 2025, pp. 1–6.

[8] J. Ding, I. Chih-Lin, J. Wang, and H. Yang, "NOMA visible light communications with distinct optical beam configurations," in *Proc. Photonics*, 2024, vol. 11, no. 10, p. 944.

[9] M. Petkovic, T. Devaja, D. Vukobratovic, F. J. Escribano, and C. Stefanovic, "Reliability analysis of slotted ALOHA with capture for an OWC-based IoT system," in *Proc. 17th Int. Symp. Wireless Commun. Syst. (ISWCS)*, Sep. 2021, pp. 1–6.

[10] D. Vukobratovic and F. J. Escribano, "Adaptive multi-receiver coded slotted ALOHA for indoor optical wireless communications," *IEEE Commun. Lett.*, vol. 24, no. 6, pp. 1308–1312, Jun. 2020.

[11] T. Devaja, M. Petković, F. J. Escribano, Č. Stefanović, and D. Vukobratović, "Slotted ALOHA with capture for OWC-based IoT: Finite block-length performance analysis," *IEEE Access*, vol. 11, pp. 76804–76815, 2023.

[12] W. Mei, X. Wei, B. Ning, Z. Chen, and R. Zhang, "Movable-antenna position optimization: A graph-based approach," *IEEE Wireless Commun. Lett.*, vol. 13, no. 7, pp. 1853–1857, Jul. 2024.

[13] X. Shao et al., "A tutorial on six-dimensional movable antenna for 6G networks: Synergizing positionable and rotatable antennas," *IEEE Commun. Surveys Tuts.*, vol. 28, pp. 3666–3709, 2026.

[14] T. Chu et al., "Revolutionizing 6G: Experimental validation of an optical integrated communication, sensing, and power transfer system," *IEEE J. Sel. Areas Commun.*, vol. 44, pp. 689–701, 2026.

[15] D. Wang, A. Elzanaty, and M.-S. Alouini, "Age-optimized irregular repetition slotted ALOHA with adaptive coding: Design and analysis," *IEEE Trans. Wireless Commun.*, vol. 25, pp. 9360–9374, 2026.